

Article

Purcell's Three-Link Swimmer: Assessment of Geometry and Gaits for Optimal Displacement and Efficiency

Cristina Nuevo-Gallardo , José Emilio Traver , Inés Tejado  and Blas M. Vinagre 

Industrial Engineering School, University of Extremadura, 06006 Badajoz, Spain; jetraverb@unex.es (J.E.T.); itejbal@unex.es (I.T.); bvinagre@unex.es (B.M.V.)

* Correspondence: cnuevog@unex.es

Abstract: This paper studies the displacement and efficiency of a Purcell's three-link microswimmer in low Reynolds number regime, capable of moving by the implementation of a motion primitive or gait. An optimization is accomplished attending to the geometry of the swimmer and the motion primitives, considering the shape of the gait and its amplitude. The objective is to find the geometry of the swimmer, amplitude and shape of the gaits which make optimal the displacement and efficiency, in both an individual way and combined (the last case will be referred to as multiobjective optimization). Three traditional gaits are compared with two primitives proposed by the authors and other three gaits recently defined in the literature. Results demonstrate that the highest displacement is obtained by the Tam and Hosoi optimal velocity gait, which also achieves the best efficiency in terms of energy consumption. The rectilinear and Tam and Hosoi optimal efficiency gaits are the second optimum primitives. Regarding the multiobjective optimization and considering the two criteria with the same weight, the optimum gaits turn out to be the rectilinear and Tam and Hosoi optimal efficiency gaits. Thus, the conclusions of this study can help designers to select, on the one hand, the best swimmer geometry for a desired motion primitive and, on the other, the optimal method of motion for trajectory tracking for such a kind of Purcell's swimmers depending on the desired control objective.

Keywords: low Reynolds number; non-reciprocal motion; displacement; efficiency; optimal; design; multiobjective optimization; gaits; Purcell's microswimmer



Citation: Nuevo-Gallardo, C.; Traver, J.E.; Tejado, I.; Vinagre, B.M. Purcell's Three-Link Swimmer: Assessment of Geometry and Gaits for Optimal Displacement and Efficiency. *Mathematics* **2021**, *9*, 1088. <https://doi.org/10.3390/math9101088>

Academic Editor: António M. Lopes

Received: 9 April 2021

Accepted: 6 May 2021

Published: 12 May 2021

Publisher's Note: MDPI stays neutral with regard to jurisdictional claims in published maps and institutional affiliations.



Copyright: © 2021 by the authors. Licensee MDPI, Basel, Switzerland. This article is an open access article distributed under the terms and conditions of the Creative Commons Attribution (CC BY) license (<https://creativecommons.org/licenses/by/4.0/>).

1. Introduction

Advances in micro- and nanotechnology have promoted the manufacturing of new miniature biomimetic artificial devices inspired by biological systems. New applications emerge due to their ability to access to small spaces at the microscale, such as perform medical procedures in a minimally invasive way, deliver drugs with high precision, and sensing towards diagnosis and monitoring [1–4]. In this sense, understanding hydrodynamics at the microscale is crucial, which implies navigating in low Reynolds number (Re) regime where viscous forces predominate over inertial ones. In this regime, the study of microswimmer dynamics acquires an important role on understanding the motion and finding new ways to propel these swimmers.

Mainly, two ways of propulsion at low Re regime can be distinguished [5]. On the one hand, the movement can be obtained by performing a unidirectional body motion, deployed by a rotating corkscrew and based on the movement of prokaryotic cells or bacteria [6]. On the other hand, flexible flagellums of eucaryotic cells have inspired the movement through planar waveforms, leading to the study of different waveforms for propulsion [7–10] and design of prototypes [11,12]. In this respect, Purcell introduced the so-called Purcell's three-link swimmer [5], composed of three links attached by one degree-of-freedom joints and defined as the simplest swimmer that could implement a gait or motion primitive within a low Re flow and manage to move a certain distance. It must

be said that there are other types of Purcell's swimmers depending on the number of links that they are made of (widely called N-link swimmers) [13,14].

Concerning the Purcell's three-link swimmer, several authors already studied its dynamics comparing the displacement obtained through the implementation of traditional primitives and estimating a coefficient of efficiency based on the energy consumption of the joints [15]. Other works study the dynamics of a 3D model and provide new gaits [16], while others analyze the dynamics of the generalized case of N-link and try to approximate it to a sperm cell swimmer [13]. Regarding the motion primitives, methods for designing new motion primitives have been reported in [14,17–19], providing the definition and implementation of different gaits, while other works analyze the symmetries of the Purcell's three-link swimmers and their effect on generating gaits with particular symmetries in order to achieve a desired net motion [20]. These symmetries allowed to define other stroke sequences, represented as a Fourier Series, which provide optimal efficiency and velocity of the swimmer [21]. Finally, the controllability of the Purcell's swimmers was studied in [13,14,16,22] and experimental trajectory tracking was addressed in [18,23]. Although considerable work has been done in this field, the defined gaits have not been compared among them, nor any study involving the displacement and efficiency has been carried out with all the motion primitives. In addition, the parameters that influence the movement of Purcell's swimmer have barely been analyzed.

This work aims to solve these research gaps offering a novel comparative study between gaits in terms of displacement and efficiency towards doing optimal both the geometric design and the trajectory tracking in future works.

This work aims to solve this research gaps offering a novel comparative study between gaits with the objective of optimizing the displacement and efficiency towards the implementation of an optimal trajectory tracking and the design of a prototype in future works. The study focuses on three aspects: the shape and amplitude of the motion primitives, and the swimmer geometry. With the purpose of analyzing the performance from different viewpoints, displacement and efficiency of the Purcell's three-link microswimmer are reported here in two different ways, namely separately and altogether, this last case by a multiobjective optimization. Regarding the motion primitives, this work proposes two new gaits and compares them with three traditional ones, already studied in the references [13–16,18,20], and other three gaits defined by other authors [19,21]. The results of this study will provide the optimal primitive along with its best amplitude and geometry of the swimmer for achieving optimal displacement, optimal efficiency and minimizing a multiobjective function. A preliminary work can be found in [24], where the displacement and efficiency were calculated for different primitives, amplitudes and geometries, although these variables were not analyzed together.

The document is organized as follows. Section 2 recalls the environment properties and the hydrodynamics related to low Re regime, based on the Navier–Stokes equations, as well as the basis of the resistive force theory (RFT). Section 3 addresses the dynamics of Purcell's three-link swimmers and introduces the gaits analyzed in this work. The optimization of displacement and efficiency is carried out in Section 4, where the two criteria are calculated depending on the shape of the gait, its amplitude, and the geometry of the swimmer. The main conclusions of this work are drawn in Section 5.

2. Background

This section describes the hydrodynamics in the microscale and the estimation of drag forces for the Purcell's swimmer.

2.1. Environment Properties

Prior to the study of the movement of Purcell's three-link swimmer, some hydrodynamics concepts are introduced to understand the movement at the microscale.

A moving fluid is characterized by Re , which determines the influence of viscous and inertial forces through the expression:

$$Re = \frac{vl\rho}{\mu} \quad (1)$$

where v and l are the maximum velocity and a characteristic dimension of the flow, respectively, and ρ and μ are the density and the dynamic viscosity of the fluid, respectively. This expression is appropriate for a Newtonian fluid, which dynamic viscosity is constant for every conditions.

Due to the dimensions of ducts and objects, the microscale is characterized by a low Re regime, which is called *slow viscous flow* and implies that the viscous forces are dominant while inertial forces are negligible [25].

On another note, the Navier–Stokes equations are essential for studying the hydrodynamics in a fluid. The expression for a Newtonian and incompressible fluid is [25,26]:

$$\rho \frac{D\mathbf{v}}{Dt} = \rho \left(\frac{\partial \mathbf{v}}{\partial t} + \mathbf{v} \cdot \nabla \mathbf{v} \right) = -\nabla p + \mu \nabla^2 \mathbf{v} + \rho \mathbf{f} \quad (2)$$

where D/Dt is the material derivative, defined as $(\frac{\partial}{\partial t} + \mathbf{v} \cdot \nabla)$. The term $\rho \frac{D\mathbf{v}}{Dt}$ represents the inertia effects, ∇p is the pressure gradient present in the fluid, $\mu \nabla^2 \mathbf{v}$ represents the diffusion and internal forces, and \mathbf{f} denotes other external forces.

As stated before, in low Re regime the inertial forces are negligible, and the Navier–Stokes equations transform into the Stokes equations [25]:

$$\mu \nabla^2 \mathbf{v} + \rho \mathbf{f} = \nabla p \quad (3)$$

On the other hand, the law of conservation of mass can be applied to any stationary volume element within a flowing fluid [25], resulting in the equation of continuity $\frac{\partial \rho}{\partial t} = -\nabla \cdot (\rho \mathbf{v})$. For an incompressible fluid, the equation can be simplified to $\nabla \cdot \mathbf{v} = 0$, where $\nabla \cdot \mathbf{v}$ is the net rate of flux. This simplification along with the Stokes equations establish the creeping motion equations for low Re regime [25]. If Re is small, it is permissible to say that there are no external forces applied to the swimmer and the fluid surrounding it. Thus, the external forces term of Stokes equations can be omitted, and the equations adopt the quasi-static form:

$$\begin{aligned} \mu \nabla^2 \mathbf{v} &= \nabla p \\ \nabla \cdot \mathbf{v} &= 0 \end{aligned} \quad (4)$$

The first consequence of low Re regime governed by the Stokes equations is the reversibility of a flow: fluid particles follow the same trajectories as a moving body within the fluid, which implies that a swimmer moving to a position and then returning by reversing the same sequence of shapes does not produce net displacement of the swimmer. This was first introduced by Purcell through the ‘scallop theorem’ [5], and consequently, a non-reciprocal motion has to be performed. The difference between reciprocal and non-reciprocal motion applied to a Purcell’s three-link swimmer is illustrated in Figure 1. The selection of an optimal non-reciprocal sequence is crucial for the Purcell’s three-link swimmer in the environment under study, as it has been proved that the net displacement only depends on the geometrical sequence of shape [27].

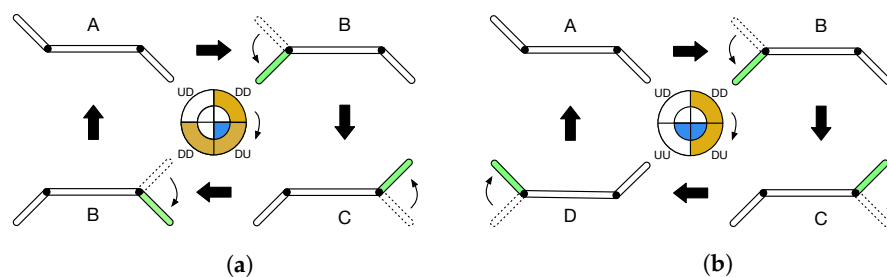


Figure 1. Types of movement of a Purcell's three-link swimmer: (a) reciprocal (b) non-reciprocal.

2.2. Drag Forces by Resistive Force Theory

In addition to the non-reciprocal motion, a moving body within a fluid needs to compensate the reactions opposing the direction of movement to generate a net displacement. These reactions are drag forces and appear longitudinal and tangentially to the direction of displacement [28].

The estimation of drag forces in low *Re* regime was studied by several authors, leading to the definition of theories and methods that apply different conditions to the object under study (see e.g., [29] and references therein). The main theories applied to the Purcell's swimmer are RFT and the slender body theory (SBT). The choice of one or the other is explained hereunder.

First, RFT estimates the drag forces acting on a slender body proportionally to its instantaneous velocity relative to the fluid and the drag coefficients, which are strictly defined by the geometry of the body and the viscosity of the fluid [28,30]. Conversely, SBT approximates the effects of a solid within a flow by a distribution of singularities, taking advantage of the slenderness of the body [31–36]. RFT and SBT were compared in [37] and the conclusions pointed out that the results obtained by RFT are consistent with those obtained by SBT in the case that no cell body is attached to the end of the body or if it is of small diameter (hence, it does not affect to the results). This conclusion leads to the application of RFT in the present work, as it is sufficient and generates consistent results, also avoiding the computational efforts of executing SBT analysis. The fundamentals of RFT are introduced hereunder.

Consider an infinitesimal element of length *ds* belonging to a slender body in an incompressible and low *Re* fluid. RFT establishes that the tangential and normal reactions of the fluid depend on the drag coefficients (*c_t* and *c_n*, respectively), on the velocity of the object in the direction of *X* or *Y* axis (*ẋ* or *ẏ*), and on the inclination angle of *ds* with respect to the horizontal (*θ_i*). Three situations may be differentiated here: the body moves in the *X* axis, in the *Y* axis, and a combination of velocities in both axis.

The reactions applied to the infinitesimal element when the body is moving with a velocity *ẋ* are illustrated in Figure 2a, being *df_{t,x}* and *df_{n,x}* the tangential and normal reactions of the fluid. A similar situation is found when the body moves in the *Y* axis (Figure 2b). Depending on the direction of the swimmer velocity, the forces of the infinitesimal element are given by [28]:

$$\text{Velocity in X axis} \begin{cases} df_{n,x}(s) = c_n \dot{x} \sin(\theta_i) ds \\ df_{t,x}(s) = c_t \dot{x} \cos(\theta_i) ds \end{cases} \quad (5)$$

$$\text{Velocity in Y axis} \begin{cases} df_{n,y}(s) = c_n \dot{y} \cos(\theta_i) ds \\ df_{t,y}(s) = c_t \dot{y} \sin(\theta_i) ds \end{cases} \quad (6)$$

When the motion is produced by a combination of velocities in *X* and *Y* directions (Figure 2c), the total forces acting normally and tangentially to the infinitesimal element are:

$$\text{Combination of velocities} \begin{cases} df_n(s) = df_{n,y}(s) - df_{n,x}(s) = c_n (\dot{y} \cos(\theta_i) - \dot{x} \sin(\theta_i)) ds \\ df_t(s) = df_{t,y}(s) + df_{t,x}(s) = c_t (\dot{y} \sin(\theta_i) + \dot{x} \cos(\theta_i)) ds \end{cases} \quad (7)$$

Details are given in [38]. The resultant forward thrust in X and Y directions is given by:

$$\begin{aligned} \mathbf{df}_x(s) &= (df_n(s) \sin(\theta_i) - df_t(s) \cos(\theta_i))\mathbf{i} \\ \mathbf{df}_y(s) &= (-df_n(s) \cos(\theta_i) - df_t(s) \sin(\theta_i))\mathbf{j} \end{aligned} \tag{8}$$

being \mathbf{i} and \mathbf{j} unit vectors in X and Y directions, respectively. The total drag force $\mathbf{dF}(s)$ applied to an infinitesimal element is the sum of forces $\mathbf{df}_x(s)$ and $\mathbf{df}_y(s)$. The torque exerted due to the calculated reactions, denoted as dm , can be estimated through the cross product of $\mathbf{r}(s)$ and $\mathbf{dF}(s)$, being $\mathbf{r}(s)$ the position of the infinitesimal element from the origin. In accordance with the above equations, the element ds can only exert a positive forward thrust if $\dot{y} > \dot{x} \tan(\theta_i)$ and $c_n > c_t$ [38].

The drag force and torque applied to a complete segment can be estimated by integrating the force and torque applied to ds through the total length of the segment (l_i):

$$\begin{aligned} \mathbf{F}_i &= \int_0^{l_i} \mathbf{dF}_i(s) ds = \int_0^{l_i} (\mathbf{df}_{x,i}(s) + \mathbf{df}_{y,i}(s)) ds \\ m_i &= \int_0^{l_i} \mathbf{r}(s) \times \mathbf{dF}_i(s) ds \end{aligned} \tag{9}$$

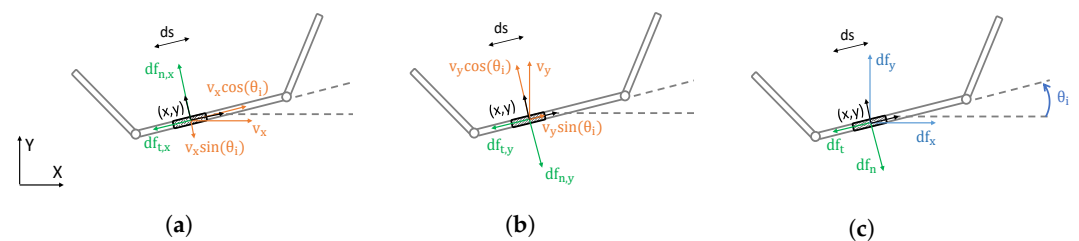


Figure 2. Fluid reactions applied to an infinitesimal element, defined by RFT: (a) motion in X axis (b) motion in Y axis (c) total drag forces.

3. Purcell’s Three-Link Swimmer

In this section, the geometry and dynamics of the Purcell’s three-link swimmer are introduced, as well as the motion primitives.

3.1. Geometry

The Purcell’s three-link swimmer consists of three links connected by one degree-of-freedom joints. In this work, the links are supposed cylindrical although another geometry can be considered. The assessment of the swimmer’s dynamics developed in this section takes as a reference the scheme shown in Figure 3.

The lengths of the links are l_0, l_1 and l_2 , while the rotary joints are designated as j_1 and j_2 . The lateral links are supposed of equal length ($l_1 = l_2$) and a ratio is defined to relate the lengths of the links ($\eta = l_0/l$, being l the total length of the swimmer). Regarding the angular positions of the links, θ_i represents the angular position of the i th link with respect to X axis of the global reference frame. The rotation of the lateral links is determined by a motion primitive or gait, which defines the angles ϕ_1 and ϕ_2 with respect to the body-fixed reference frame (x, y) . The relations between the angular position and the gait angles are $\theta_1 = \phi_1 - \theta_0$; and $\theta_2 = \phi_2 + \theta_0$. The position of the center of i th link is defined as $\mathbf{X}_i = (x_i \ y_i \ \theta_i)^T$.

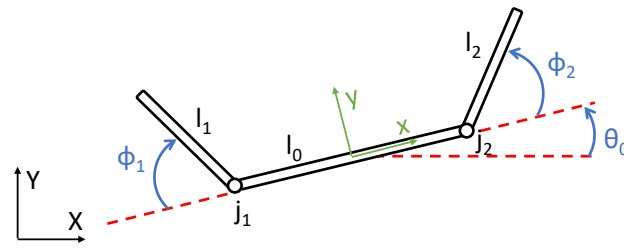


Figure 3. General scheme of the Purcell’s three-link swimmer.

3.2. Dynamics

Next, the displacement of the central (or base) link of Purcell’s three-link swimmer will be estimated. First, the planar and angular position of the three links must be analyzed. The movement of links l_1 and l_2 with respect to the central link is completely defined by angles ϕ_1 and ϕ_2 , while the position of the base link with respect to the global reference frame is unknown, designated as $\mathbf{X}_0 = (x_0 \ y_0 \ \theta_0)^T$.

The position of the lateral links with respect to the central link can be easily estimated as follows:

$$\begin{aligned} \mathbf{X}_1 &= \mathbf{X}_0 + \frac{l_0}{2} \begin{pmatrix} -\cos(\theta_0) \\ -\sin(\theta_0) \\ 0 \end{pmatrix} + \frac{l_1}{2} \begin{pmatrix} -\cos(\phi_1 - \theta_0) \\ \sin(\phi_1 - \theta_0) \\ 0 \end{pmatrix} + \begin{pmatrix} 0 \\ 0 \\ 180 - \phi_1 \end{pmatrix} \\ \mathbf{X}_2 &= \mathbf{X}_0 + \frac{l_0}{2} \begin{pmatrix} \cos(\theta_0) \\ \sin(\theta_0) \\ 0 \end{pmatrix} + \frac{l_2}{2} \begin{pmatrix} \cos(\phi_2 + \theta_0) \\ \sin(\phi_2 + \theta_0) \\ 0 \end{pmatrix} + \begin{pmatrix} 0 \\ 0 \\ \phi_2 \end{pmatrix} \end{aligned} \tag{10}$$

The position can be derived and an expression is obtained, associating the linear and angular velocities of the links ($\dot{\mathbf{X}}_i = (\dot{x}_i \ \dot{y}_i \ \dot{\theta}_i)^T$), the linear and angular velocities of the central link ($\dot{\mathbf{X}}_0 = (\dot{x}_0 \ \dot{y}_0 \ \dot{\theta}_0)^T$), and the angular velocities of the lateral links with respect to the body-fixed reference frame ($\dot{\Phi} = (\dot{\phi}_1 \ \dot{\phi}_2)^T$). This relation can be written in matrix form, achieving the following expression [15,17,20]:

$$\dot{\mathbf{X}}_i = \mathbf{T}_i(\mathbf{X}_0, \Phi) \dot{\mathbf{X}}_0 + \mathbf{E}_i(\mathbf{X}_0, \Phi) \dot{\Phi} \tag{11}$$

Matrices \mathbf{T}_i and \mathbf{E}_i are given in the reference [17] and depend on the link whose velocity is being calculated. The total drag forces and torque applied to the i th link can be calculated through RFT [15], considering $c_{ni} = 2c_{ti} = 4\pi\mu / \log(l_i/a_i)$, being a_i the radius of the i th link. The following matrix expression is achieved:

$$\mathbf{F}_i = -R_i(\mathbf{X}_0, \Phi) \dot{\mathbf{X}}_i \tag{12}$$

$$R_i(\mathbf{X}_0, \Phi) = c_{ti} l_i \begin{pmatrix} 1 + \sin^2(\theta_i) & -\cos(\theta_i) \sin(\theta_i) & 0 \\ -\cos(\theta_i) \sin(\theta_i) & 1 + \cos^2(\theta_i) & 0 \\ 0 & 0 & \frac{1}{6} l_i^2 \end{pmatrix} \tag{13}$$

where $\mathbf{F}_i = (f_{ix} \ f_{iy} \ m_i)^T$ and R_i is called the resistance tensor. The total drag forces acting on the swimmer’s body (denoted as $\mathbf{F}_b = (f_{bx} \ f_{by} \ m_b)^T$) are the summation of the forces applied to each link, and the total torque can be estimated by:

$$\mathbf{F}_b = \sum_{i=0}^2 \mathbf{T}_i^T \mathbf{F}_i = - \sum_{i=0}^2 \mathbf{T}_i^T R_i (\mathbf{T}_i \dot{\mathbf{X}}_0 + \mathbf{E}_i \dot{\Phi}) \tag{14}$$

$$m_b = \sum_{i=0}^2 (m_i + ((\mathbf{r}_j - \mathbf{r}_i) \times \mathbf{f}_i) \cdot \mathbf{k}) \tag{15}$$

where \mathbf{r}_j and \mathbf{r}_i are the positions of the j th joint and the i th link with respect to the global reference frame, respectively; $\mathbf{f}_i = (f_{ix} \ f_{iy})$ and \mathbf{k} is a unit vector in Z direction. According to a Stokes' flow, a quasi-static motion is assumed; thus, the swimmer is in static equilibrium and the total drag forces and torques acting on the swimmer's body are $\mathbf{F}_b = 0$ [15,17,20]. Substituting into (14) results in:

$$\dot{\mathbf{X}}_0 = -\frac{\sum_{i=0}^2 \mathbf{T}_i^T R_i \mathbf{E}_i}{\sum_{i=0}^2 \mathbf{T}_i^T R_i \mathbf{T}_i} \dot{\Phi} \tag{16}$$

To solve the differential Equation (16) and estimate the position of the central link, the Runge–Kutta method is applied. The results obtained are plotted in Figure 4, which match those presented in [13,39].

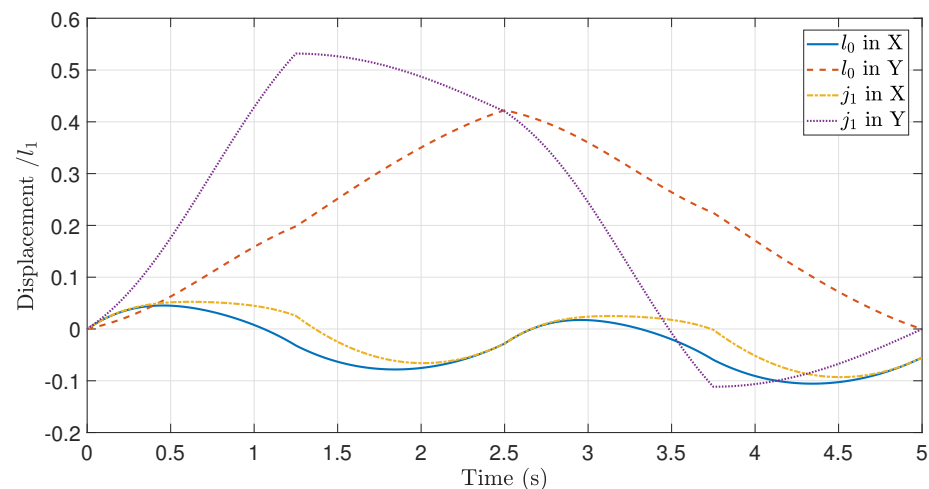


Figure 4. Normalized displacement of the central link (l_0) and left joint (j_1) of the Purcell's three-link swimmer in X and Y axis, implementing a square gait with $\pi/3$ as its amplitude, $\eta = 1/2$, $l_0 = 2$ and $l = 4$. The results match those presented in [13,39].

3.3. Motion Primitives

As a consequence of the reversibility of the flow in low Re regime, a non-reciprocal motion must be performed towards a net displacement of the swimmer, which can be fulfilled by the application of a motion primitive or gait. As above-mentioned, a gait determines the movement of links l_1 and l_2 through the angles ϕ_1 and ϕ_2 . The definition of a gait has been considered to be as follows:

$$\phi_1 = \epsilon s_1; \ \phi_2 = \epsilon s_2 \tag{17}$$

where s_1 and s_2 are the angles with unitary amplitude, and ϵ is the gait amplitude. The shape of a motion primitive determines the displacement reached by the Purcell's swimmer, so the analysis of different gaits plays a key role to be able to choose the most appropriate.

The gaits analyzed in this work are shown in Figure 5 and have been selected following the criteria found in the literature. The square gait is the most common primitive [13–15,20,21], followed up by a figure-eight shape (called rectilinear henceforth) [16,18,20] and circular [15]. The gaits in the second row of Figure 5 have been defined in [19,21] as optimal gaits, while the remaining motion primitives are proposed by the authors and were defined by inspiration from the others, and whose definition can be found in Appendix A.

These gaits are divided into two types: consecutive (Figure 5a,b) and simultaneous (the rest). The consecutive gaits are characterized by an alternate movement of the links, i.e., only one link is moving at once. On the other hand, the simultaneous gaits are defined by links constantly moving.

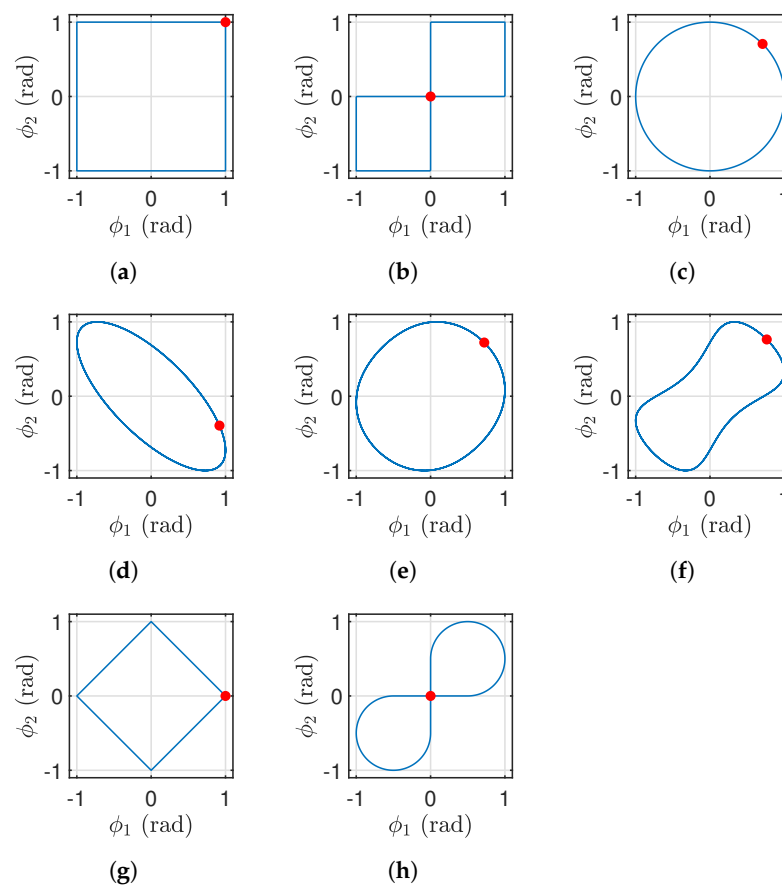


Figure 5. Different gaits applied to the Purcell’s swimmer, with unitary amplitude: (a) square (b) rectilinear (c) circular (d) Alouges optimal gait from [19] (e) optimal efficiency gait from [21] (f) optimal velocity gait from [21] (g) diamond gait (h) petal gait. The coloured circular mark represents the initial point of the gait.

Despite every gait has two versions depending on the direction followed by the angles (clockwise or counterclockwise), it has been proved that the net displacement does not depend on the direction of the gait. In fact, the displacements achieved are identical in magnitude but opposite in sign. It is important to remark that motion primitives in Figure 5 only produce net movement in X axis, thus, displacement in this direction will be studied further on.

4. Optimization of Displacement and Efficiency According to the Shape and Amplitude of the Gaits and the Geometry of the Swimmer

This section presents the results of a comparative study in which the variables to optimize are the displacement of the swimmer, solving the differential Equation (16), and the energy consumption of the joints through a coefficient of efficiency (defined further on). The latter has been considered in this work since the implementation of a gait may achieve the highest displacement while increases the energy consumption, and this must be taken into consideration, especially for trajectory tracking.

The parameters that may affect the displacement of the swimmer are the gait amplitude (ϵ), the relation between lengths of the links (η), the total length of the swimmer (l), the radius of the links (a), the gait period (T_g), and the viscosity of the fluid (μ). The displacement varying these parameters is plotted in Figure 6. As a resume, the radius, the gait period and the viscosity do not influence the displacement (Figure 6d–f), considering the range of values of the figure, which have been chosen as the most suitable ones in the scale where the swimmer would navigate. On the other hand, the displacement and the total length of the swimmer have a proportional relation (Figure 6c), which implies that the

longer the swimmer, the higher the achieved displacement. Finally, the gait amplitude and the relation between lengths of the links have a major impact on the displacement, and thus, have been considered in the comparative study along with the shape of the gait. The gait amplitude is within the range $[0, \pi]$ due to physical restrictions and to extend the limits considered in [24].

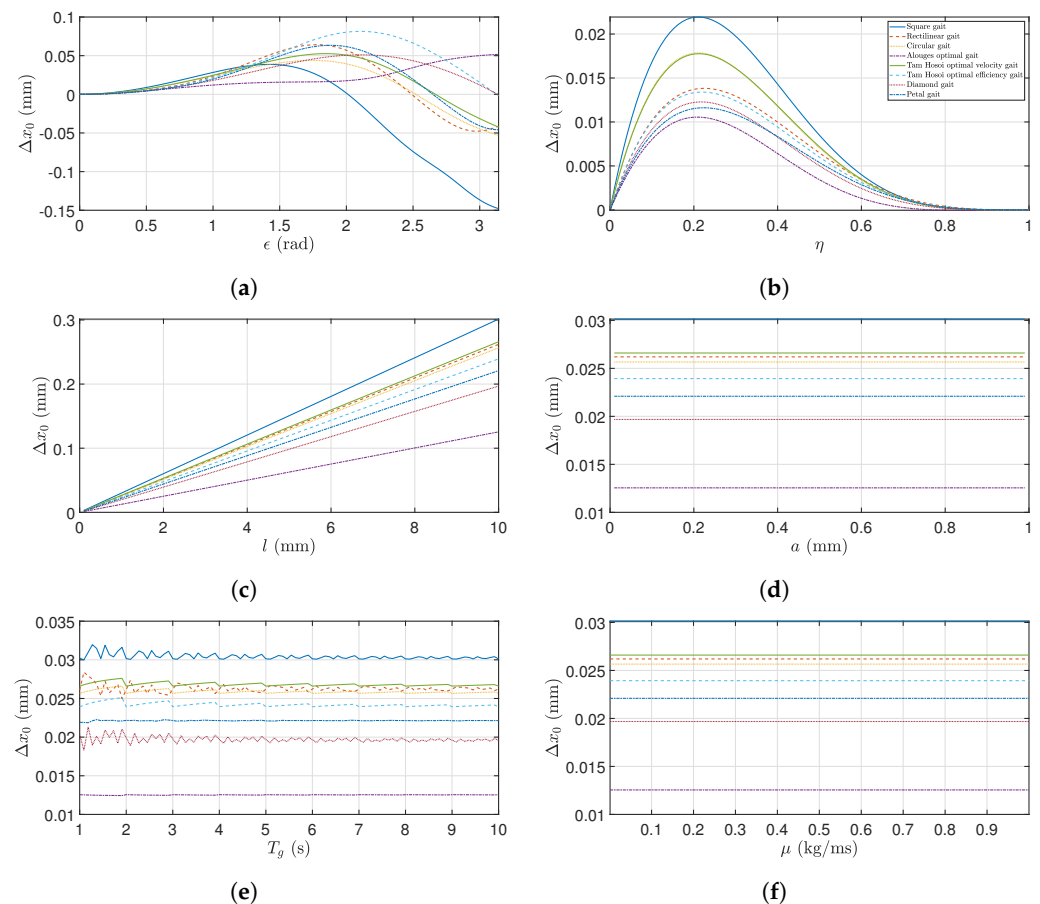


Figure 6. Displacement of the Purcell’s three-link swimmer depending on several parameters which may influence its movement: (a) amplitude of the gait (ϵ) (b) relation between lengths of the links ($\eta = l_0/l$) (c) radius of the links (a) (d) total length of the swimmer (l) (e) gait period (T_g) (f) viscosity of the fluid (μ).

The results included in the following subsections have been obtained with MATLAB[®] and were calculated considering a millimeter size of the robot ($l = 1$ mm). The radius of the links is also assumed small ($a = 0.25$ mm), and the fluid in which the swimmer would navigate is a silicone oil characterized by a viscosity $\mu = 0.0964$ kg/(m·s), meeting the requisites of low Re regime and selected for future in-lab experiments.

4.1. Optimal Displacement

The first parameter to be analyzed is the displacement of the swimmer. The calculations have been carried out varying both the gait amplitude and the relation between lengths of the links, obtaining a data array that can be plotted in 3D as shown in Figure 7a. From these data, the maximum values of displacement can be extracted, which are tabulated in Table 1 in order of decreasing displacement. For additional information and to resume the results, the data from Table 1 is also displayed in Figure 7b.

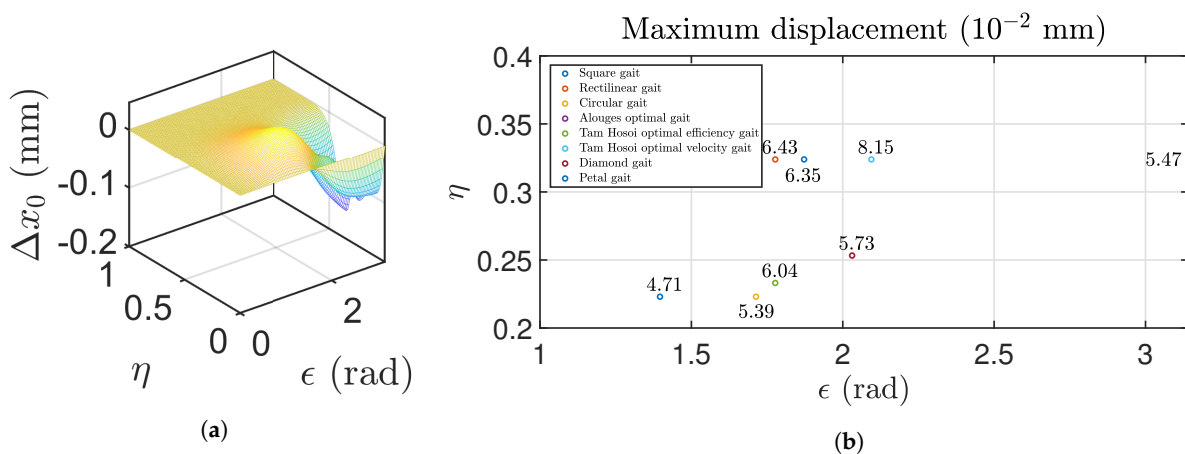


Figure 7. Results for optimal displacement: (a) 3D plot of displacement applying the square gait to the Purcell’s three-link swimmer, (b) maximum values of displacement with their corresponding gait amplitude (ϵ) and relation between lengths of the links (η).

As it can be extracted from the results, the maximum displacement is achieved for values of $1.4 \text{ rad} < \epsilon < 2.1 \text{ rad}$ and $0.2 < \eta < 0.4$. However, there is a maximum out of these limits, corresponding to the Alouges optimal gait from [19], which reaches the maximum value of displacement for $\epsilon = \pi \text{ rad}$. It should be evaluated if this gait amplitude is possible to be implemented or, due to physical restrictions, such amplitude is not suitable and must be neglected. This gait does not present any other optimal points in the range under study, so the unique optimal displacement corresponds to this point. The amplitude limits should be taken into account to select the most appropriate primitive, as all the analyzed gaits exhibit similar results and achieve the maximum displacement for amplitudes higher than 1.57 rad.

On the other hand, Table 1 provides the Tam and Hosoi optimal velocity gait from [21] as the optimal one taking into account the displacement, as the Purcell’s swimmer can reach a distance of $81.5 \mu\text{m}$ through the implementation of this gait. The next three gaits in Table 1 present similar displacements around 60 and $65 \mu\text{m}$. These primitives are rectilinear, petal and Tam and Hosoi optimal efficiency gait from [21], in order of decreasing displacement. The worst primitive in this case is the square one, providing a displacement of $47 \mu\text{m}$. As it can be observed, the first gait reaches two times the displacement of the square gait.

Table 1. Optimal values of gait amplitude (ϵ) and relation between lengths of the links (η) for maximum displacement. The data are sorted in order of decreasing displacement.

Gait	$\Delta x_{0,max} \cdot 10^{-2}$ (mm)	ϵ	η
Tam Hosoi optimal velocity gait	8.15	2.09	0.3239
Rectilinear	6.43	1.78	0.3239
Petal	6.35	1.87	0.3239
Tam Hosoi optimal efficiency gait	6.04	1.78	0.2331
Diamond	5.73	2.03	0.2533
Alouges optimal gait	5.47	π	0.3239
Circular	5.39	1.71	0.2230
Square	4.70	1.39	0.2230

4.2. Optimal Efficiency

Once the displacement has been calculated, the energy consumption of the joints must be taken into consideration to develop a suitable optimization study, as the Purcell’s swimmer may achieve the highest displacement while increases the energy consumption. This is highly important for trajectory tracking and for the choice of the best non-reciprocal motion.

A useful criterion to evaluate the energy consumption versus the displacement achieved is a coefficient of efficiency, which can be estimated for a Purcell’s three-link swimmer as [15,21,31,39]:

$$\zeta = \frac{c_t l \bar{x}_0^2}{P} \tag{18}$$

being \bar{x}_0 the average velocity of the center of link l_0 , and P the average mechanical power deployed by the joints, calculated through $P = -\sum_{i=0}^2 \mathbf{F}_i^T \dot{\mathbf{X}}_i$ [15].

As performed in the previous subsection, the efficiency is calculated varying both the gait amplitude and the relation between lengths of the links. As it can be observed from Figure 6a, the majority of the gaits reaches the highest displacement at a turning point and, from then on, the displacement decreases while the gait amplitude rises. In this work, only positive displacements in X axis are considered, so the values of efficiency that correspond to negative displacement will be neglected.

From the data array obtained, the maximum values of efficiency can be extracted, which are tabulated in Table 2 along with their corresponding gait amplitude and relation between lengths of the links. Additionally, Figure 8b shows the same data in a plot. As it can be extracted from this figure, the maximum efficiency is reached for values of $1 \text{ rad} < \epsilon < 2 \text{ rad}$ and $0.2 < \eta < 0.4$, which are similar to those of the maximum displacement in the previous section.

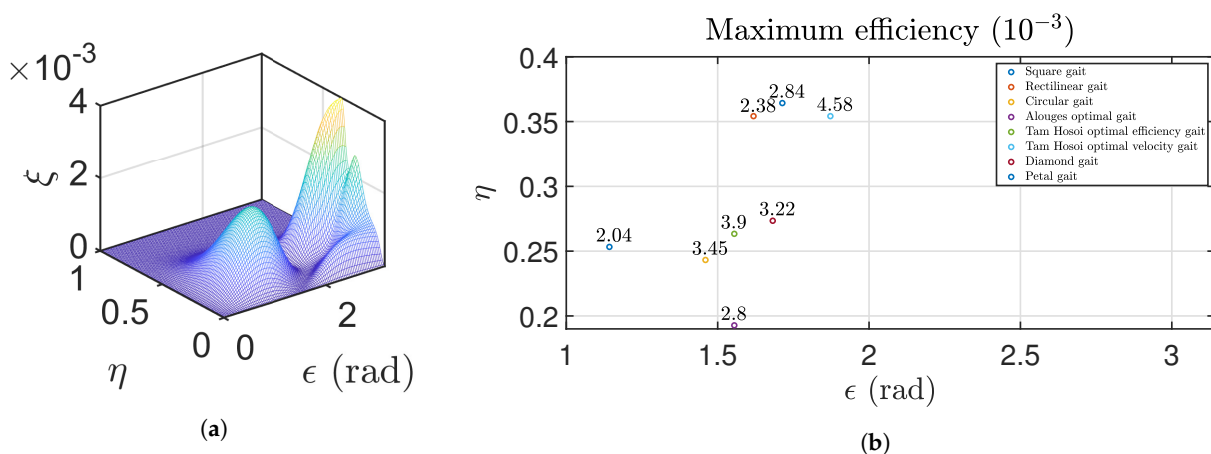


Figure 8. Results for optimal efficiency: (a) 3D plot of efficiency applying the square gait to the Purcell’s three-link swimmer, (b) maximum values of efficiency with their corresponding gait amplitude (ϵ) and relation between lengths of the links (η).

Table 2. Optimal values of gait amplitude (ϵ) and relation between lengths of the links (η) for maximum efficiency. The data are sorted in order of decreasing efficiency.

Gait	$\zeta_{max} \cdot 10^{-3}$	ϵ	η
Tam Hosoi optimal velocity gait	4.6	1.87	0.3542
Tam Hosoi optimal efficiency gait	3.9	1.55	0.2634
Circular	3.4	1.46	0.2432
Diamond	3.2	1.68	0.2735
Alouges optimal gait	2.8	1.55	0.1927
Petal	2.8	1.71	0.3643
Rectilinear	2.4	1.62	0.3542
Square	2.0	1.14	0.2533

Regarding the classification in Table 2, the most efficient primitive matches the one that allows obtaining the highest displacement, i.e., the Tam and Hosoi optimal velocity gait from [21]. The primitive is followed up by the Tam and Hosoi optimal efficiency gait, in the second place, and the circular and diamond primitives, in third and fourth place. The last gait is, again, the square one.

4.3. Multiobjective Optimization

In the previous subsections, separated optimizations have been carried out considering the displacement and the efficiency as the objectives to maximize. In order to complete the study, these two criteria previously defined are considered at the same time through a multiobjective optimization.

The optimization problems can be classified through the number of decision variables, the type of decision variable, the type of objective function, and the form of the problem. If the problem has more than one objective to be satisfied, it is called multiobjective or multicriteria optimization problem. Within the multiobjective optimization methods, the following classification divides the methods into five groups [40,41]:

1. Scalar methods: transform the multiobjective problem into a mono-objective problem.
2. Interactive methods: sequential processes composed of several iterations.
3. Fuzzy methods: involving fuzzy logic.
4. Multiobjective methods using metaheuristics: they are stochastic methods, designed to solve difficult optimization problems by means of an intuitive approach.
5. Decision aid methods: based on the establishment of an orderly relationship between the different actions or solutions.

The scalar methods will be used in this work, due to their simplicity. Moreover, within the scalar methods, the weighted-sum-of-objective-functions method will be accomplished, in which each criterion or subfunction is associated with a weight and, then, the main objective function is defined as a weighted sum of the objective subfunctions [40]. Usually, the optimization method includes a minimization of the objective function. For that purpose, the new objective function must be defined as follows:

$$\text{minimize } G(x) = \sum_{i=1}^k \omega_i g_i(x) \quad , \quad \sum_{i=1}^k \omega_i = 1 \quad | \quad \omega_i > 0 \quad (19)$$

where ω_i are the weights associated with each criterion g_i and k is the number of objectives. In this case, the subfunctions g_i are the displacement and efficiency relative errors with respect to their maximum values, defined as:

$$g_1(\mathbf{X}_0, \Phi) = x_{error}(\mathbf{X}_0, \Phi) = \frac{\Delta x_{max} - \Delta x_i}{\Delta x_{max}} \quad (20)$$

$$g_2(\mathbf{X}_0, \Phi) = \zeta_{error}(\mathbf{X}_0, \Phi) = \frac{\zeta_{max} - \zeta_i}{\zeta_{max}} \quad (21)$$

Combining the above equations and considering $\omega_2 = 1 - \omega_1$, the objective function (19) is:

$$\begin{aligned} \text{minimize } G(\mathbf{X}_0, \Phi) &= \omega_1 g_1(\mathbf{X}_0, \Phi) + \omega_2 g_2(\mathbf{X}_0, \Phi) \\ &= \omega_1 \frac{\Delta x_{max} - \Delta x_i}{\Delta x_{max}} + (1 - \omega_1) \frac{\zeta_{max} - \zeta_i}{\zeta_{max}} \end{aligned} \quad (22)$$

The last step consists of defining the weight ω_1 . The optimization can be carried out with the aim of finding the optimal values for the weights, but in this case, both criteria g_1 and g_2 wish to have the same importance in the multiobjective optimization. Thus, the weights are chosen as $\omega_1 = \omega_2 = 0.5$.

As in the previous analyses, a data array is obtained (plotted in 3D in Figure 9a) and the minimum value of the function can be extracted. Table 3 summarizes the minimum values of $G(s)$ along with their corresponding gait amplitude and relation between lengths of the links, being the data sorted in order of increasing function value. The results are also shown graphically in Figure 9b.

The results in Figure 9b show that the primitives are optimal in the range $1.2 \text{ rad} < \epsilon < 2 \text{ rad}$ and $0.2 < \eta < 0.4$, similar to the previous criteria of displacement and

efficiency. Moreover, considering the results in Table 3, the rectilinear gait is the optimum one, followed up by the Tam and Hosoi optimal efficiency gait in [21], petal gait and Tam and Hosoi optimal velocity gait. The order of the primitives differs from that in previous criteria, as now the Tam and Hosoi optimal velocity gait is not the optimal primitive and the worst primitive is the Alouges optimal gait in [19].

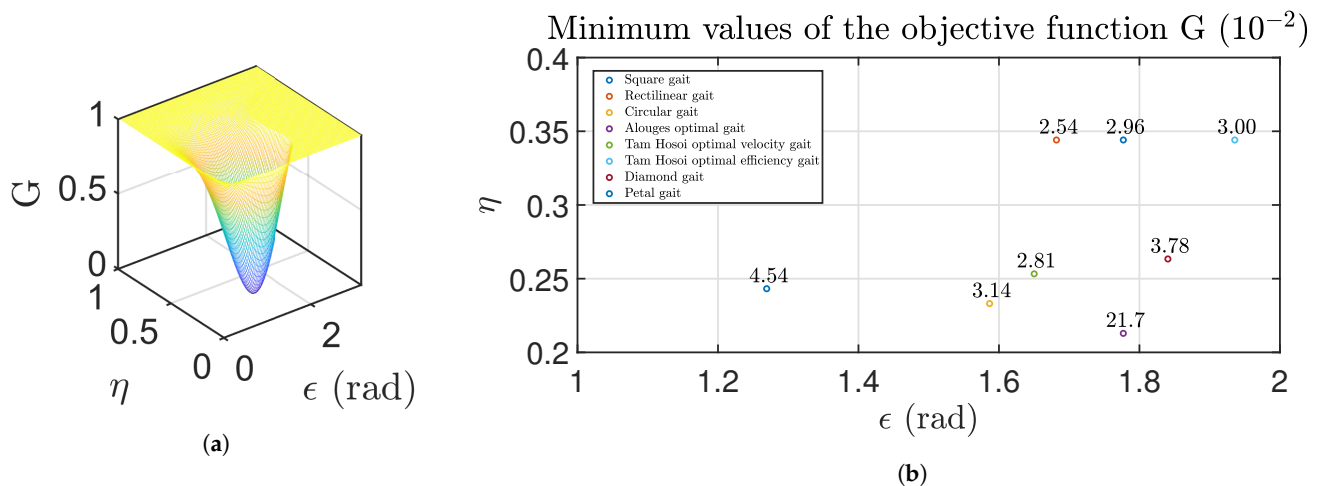


Figure 9. Results from optimal objective function: (a) 3D plot of the objective function applying the square gait, (b) minimum values of the objective function with their corresponding gait amplitude (ϵ) and relation between lengths of the links (η).

Table 3. Optimal values of gait amplitude (ϵ) and relation between lengths of the links (η) for minimum values of the objective function. The data are sorted in order of increasing function value.

Gait	G_{min}	ϵ	η
Rectilinear	0.0254	1.68	0.3441
Tam Hosoi optimal efficiency gait	0.0281	1.65	0.2533
Petal	0.0296	1.78	0.3441
Tam Hosoi optimal velocity gait	0.0300	1.93	0.3441
Circular	0.0314	1.59	0.2331
Diamond	0.0378	1.84	0.2634
Square	0.0454	1.27	0.2432
Alouges optimal gait	0.2167	1.78	0.2129

5. Conclusions

This paper has studied the displacement and efficiency of Purcell’s three-link microswimmer in low Reynolds number regime extending the comparative study carried out in [24]. The optimization study has been accomplished attending to the geometry of the swimmer and the motion primitives, focusing on two aspects: the shape of the gait and its amplitude. For this aim, two new gaits have been designed, simulated and compared to three traditional primitives and other three optimal primitives already studied in the references.

Three procedures have been carried out. In the first two of them, the displacement and efficiency have been maximized, while a multiobjective optimization has been performed considering the two previous criteria in terms of error. Common to all the procedures, the data have been estimated varying the amplitude and geometry at the same time.

The results demonstrated that both the maximum displacement and efficiency are achieved for values of gait amplitude between 1 and 2 rad, and relation between lengths of the links ($\eta = l_0/l$) between 0.2 and 0.4. The same occurs with the multiobjective optimization.

In terms of maximum displacement, the best primitive is the Tam and Hosoi optimal velocity gait in [21], followed by the rectilinear and petal gaits, being the petal primitive

proposed by the authors. With respect to the maximum efficiency, the Tam and Hosoi optimal velocity gait is also the best one, while the Tam and Hosoi optimal efficiency gait in [21] and the circular one are in third and fourth place. Regarding assigning the same weight to both criteria, the rectilinear gait gives the optimum results, followed by the Tam and Hosoi optimal efficiency gait and the petal gait.

As a conclusion, the results of this study can be useful for selecting the optimal method of motion, with respect to the type of gait, its amplitude and even the swimmer geometry, depending on the desired control objective in trajectory tracking.

Our future works will focus on: (1) designing the optimal control for trajectory tracking of a Purcell's three-link swimmer, (2) designing and testing experimentally a Purcell's swimmer prototype, and (3) studying its controllability.

Author Contributions: This work involved all coauthors. C.N.-G. wrote the original draft and contributed to the investigation and the analysis, edited the manuscript and contributed to the illustrations. J.E.T. contributed to the illustrations and the editing. I.T. and B.M.V. conceived the idea, contributed to the editing and supervised all the manuscript. All authors have read and agreed to the published version of the manuscript.

Funding: This work has been supported in part by the Consejería de Economía, Ciencia y Agenda Digital (Junta de Extremadura) under the project IB18109 and the grant "Ayuda a Grupos de Investigación de Extremadura" (no. GR18159), and in part by the European Regional Development Fund "A way to make Europe".

Institutional Review Board Statement: Not applicable.

Informed Consent Statement: Not applicable.

Data Availability Statement: The data will be available under request.

Acknowledgments: Cristina Nuevo-Gallardo would like to thank University of Extremadura its support through the scholarship "Plan Propio de Iniciación a la Investigación, Desarrollo Tecnológico e Innovación 2019".

Conflicts of Interest: The authors declare no conflict of interest.

Abbreviations

The following abbreviations are used in this manuscript:

Re	Reynolds number
RFT	Resistive Force Theory
SBT	Slender Body Theory

Appendix A

In this appendix, the definition of the new gaits proposed in this work is provided. These primitives are diamond and petal.

The unscaled angles s_1 and s_2 for these primitives in their clockwise version are defined as piecewise functions by the following equations:

$$\text{Diamond : } s_1(t) = \begin{cases} 1 - \frac{1}{t_1}t, & t \in (0, t_1] \\ \frac{-1}{t_2 - t_1}(t - t_1), & t \in (t_1, t_2] \\ -1 + \frac{1}{t_3 - t_2}(t - t_2), & t \in (t_2, t_3] \\ \frac{1}{T_f - t_3}(t - t_3), & t \in (t_3, T_f] \end{cases}, \tag{A1}$$

$$s_2(t) = \begin{cases} \frac{-1}{t_1}t, & t \in (0, t_1] \\ -1 + \frac{1}{t_2 - t_1}(t - t_1), & t \in (t_1, t_2] \\ \frac{1}{t_3 - t_2}(t - t_2), & t \in (t_2, t_3] \\ 1 - \frac{1}{T_f - t_3}(t - t_3), & t \in (t_3, T_f] \end{cases} \tag{A2}$$

$$\text{Petal : } s_1(t) = \begin{cases} 0, & t \in (0, t_1] \\ -0.5 + 0.5 \sin\left(\frac{4\pi}{T_f}(t - t_1) + \frac{\pi}{2}\right), & t \in (t_1, t_2] \\ -0.5 + \frac{0.5}{t_3 - t_2}(t - t_2), & t \in (t_2, t_3] \\ 0, & t \in (t_3, t_4] \\ 0.5 + 0.5 \sin\left(\frac{4\pi}{T_f}(t - t_4) - \frac{\pi}{2}\right), & t \in (t_4, t_5] \\ 0.5 - \frac{0.5}{T_f - t_5}(t - t_5), & t \in (t_5, T_f] \end{cases}, \tag{A3}$$

$$s_2(t) = \begin{cases} \frac{-0.5}{t_1}t, & t \in (0, t_1] \\ -0.5 + 0.5 \cos\left(\frac{4\pi}{T_f}(t - t_1) + \frac{\pi}{2}\right), & t \in (t_1, t_2] \\ 0, & t \in (t_2, t_3] \\ \frac{0.5}{t_4 - t_3}(t - t_3), & t \in (t_3, t_4] \\ 0.5 + 0.5 \cos\left(\frac{4\pi}{T_f}(t - t_4) - \frac{\pi}{2}\right), & t \in (t_4, t_5] \\ 0, & t \in (t_5, T_f] \end{cases} \tag{A4}$$

where T_f is the final time of simulation and the segments are considered of equal duration.

References

1. Sitti, M.; Ceylan, H.; Hu, W.; Giltinan, J.; Turan, M.; Yim, S.; Diller, E. Biomedical Applications of Untethered Mobile Milli/Microrobots. *Proc. IEEE* **2015**, *103*, 205–224. [CrossRef]
2. Li, J.; Esteban-Fernández de Ávila, B.; Gao, W.; Zhang, L.; Wang, J. Micro/nanorobots for biomedicine: Delivery, surgery, sensing, and detoxification. *Sci. Robot.* **2017**, *2*, eaam6431. [CrossRef] [PubMed]

3. Medina-Sánchez, M.; Xu, H.; Schmidt, O.G. Micro- and nano-motors: The new generation of drug carriers. *Ther. Deliv.* **2018**, *9*, 303–316. [[CrossRef](#)]
4. Soto, F.; Wang, J.; Ahmed, R.; Demirci, U. Medical Micro/Nanorobots in Precision Medicine. *Adv. Sci.* **2020**, *7*, 2002203. [[CrossRef](#)]
5. Purcell, E.M. Life at low Reynolds number. *Am. J. Phys.* **1977**, *45*, 3–11. [[CrossRef](#)]
6. Silva, J.; Prieto, J.; Tejado, I.; Pérez, E.; Vinagre, B.M. Robots nadadores tipo flagelo bacteriano de pequeñas dimensiones: Desarrollo de prototipos y plataformas de prueba. In Proceedings of the XXXVII Jornadas de Automática, Madrid, Spain, 7–9 September 2016; pp. 740–747. (In Spanish)
7. Traver, J.E.; Vinagre, B.M.; Tejado, I. Robot nadador tipo flagelo bacteriano plano: Estudio y simulación del mecanismo de propulsión. In Proceedings of the XXXVII Jornadas de Automática, Madrid, Spain, 7–9 September 2016; pp. 1075–1082. (In Spanish)
8. Traver, J.E.; Tejado, I.; Vinagre, B.M. A Comparative Study of Planar Waveforms for Propulsion of a Joined Artificial Bacterial Flagella Swimming Robot. In Proceedings of the 4th International Conference on Control, Decision and Information Technologies (CoDIT'17), Barcelona, Spain, 5–7 April 2017; pp. 550–555.
9. Prieto-Arranz, J.; Traver, J.E.; López, M.A.; Tejado, I.; Vinagre, B.M. Study in COMSOL of the generation of traveling waves in an AEF robot by piezoelectric actuation. In Proceedings of the XXXIX Jornadas de Automática, Badajoz, Spain, 5–7 September 2018; pp. 748–755.
10. Traver, J.E.; Tejado, I.; Prieto-Arranz, J.; Nuevo-Gallardo, C.; Vinagre, B.M. Improved Locomotion of an AEF Swimming Robot Using Fractional Order Control. In Proceedings of the 2019 IEEE International Conference on Systems, Man, and Cybernetics (IEEE SMC 2019), Bari, Italy, 6–9 October 2019; pp. 2559–2564.
11. Traver, J.E.; Tejado, I.; Nuevo-Gallardo, C.; Prieto-Arranz, J.; López, M.A.; Vinagre, B.M., Evaluating an AEF Swimming Microrobot Using a Hardware-in-the-loop Testbed. In *Robot 2019: Fourth Iberian Robotics Conference*; Springer: Cham, Switzerland, 2020; pp. 524–536.
12. Traver, J.E.; Tejado, I.; Nuevo-Gallardo, C.; López, M.A.; Vinagre, B.M. Performance study of propulsion of N-link artificial Eukaryotic flagellum swimming microrobot within a fractional order approach: From simulations to hardware-in-the-loop experiments. *Eur. J. Control* **2021**, *58*, 340–356. [[CrossRef](#)]
13. Alouges, F.; DeSimone, A.; Giraldi, L.; Zoppello, M. Self-propulsion of slender micro-swimmers by curvature control: N-link swimmers. *Int. J. Non-Linear Mech.* **2013**, *56*, 132–141. [[CrossRef](#)]
14. Giraldi, L.; Martinon, P.; Zoppello, M. Controllability and optimal strokes for N-link microswimmer. In Proceedings of the 52nd IEEE Conference on Decision and Control, Firenze, Italy, 10–13 December 2013; pp. 3870–3875.
15. Wiezel, O.; Or, Y. Optimization and small-amplitude analysis of Purcell's three-link microswimmer model. *Proc. R. Soc. A Math. Phys. Eng. Sci.* **2016**, *472*, 4–25. [[CrossRef](#)] [[PubMed](#)]
16. Kadam, S.; Banavar, R. Geometry of locomotion of the generalized Purcell's swimmer: Modelling, controllability and motion primitives. *IFAC J. Syst. Control* **2018**, *4*, 7–16. [[CrossRef](#)]
17. Wiezel, O.; Or, Y. Using optimal control to obtain maximum displacement gait for Purcell's three-link swimmer. In Proceedings of the 2016 IEEE 55th Conference on Decision and Control (CDC), Las Vegas, NV, USA, 12–14 December 2016; pp. 4463–4468.
18. Kadam, S.; Joshi, K.; Gupta, N.; Katdare, P.; Banavar, R.N. Trajectory tracking using motion primitives for the Purcell's swimmer. In Proceedings of the 2017 IEEE/RSJ International Conference on Intelligent Robots and Systems (IROS), Vancouver, BC, Canada, 24–28 September 2017; pp. 3246–3251.
19. Alouges, F.; DeSimone, A.; Giraldi, L.; Or, Y.; Wiezel, O. Energy-optimal strokes for multi-link microswimmers: Purcell's loops and Taylor's waves reconciled. *New J. Phys.* **2019**, *21*, 043050. [[CrossRef](#)]
20. Gutman, E.; Or, Y. Symmetries and gaits for Purcell's three-link microswimmer model. *IEEE Trans. Robot.* **2016**, *32*, 53–69. [[CrossRef](#)]
21. Tam, D.; Hosoi, A.E. Optimal stroke patterns for Purcell's three-link swimmer. *Phys. Rev. Lett.* **2007**, *98*, 068105. [[CrossRef](#)] [[PubMed](#)]
22. Kadam, S.; Banavar, R.N. Geometric Controllability of The Purcell's Swimmer and its Symmetrized Cousin. *IFAC-PapersOnLine* **2016**, *49*, 988–993. [[CrossRef](#)]
23. Jaskaran Singh Grover. Geometric Approaches to Motion Planning for Two Classes of Low Reynolds Number Swimmers. Ph.D. Thesis, The Robotics Institute, School of Computer Science, Carnegie Mellon University, Pittsburgh, PA, USA, 2018.
24. Nuevo-Gallardo, C.; Traver, J.E.; Tejado, I.; Vinagre, B.M.; Rodríguez, P. Comparative study of gaits and geometry for optimal displacement and efficiency of Purcell's three-link microswimmers. In Proceedings of the 28nd Seminario Anual de Automática, Electrónica Industrial e Instrumentación, Ciudad Real, Spain, 7–9 July 2021; submitted.
25. Happel, J.; Brenner, H. *Low Reynolds Number Hydrodynamics*, 2nd ed.; Martinus Nijhoff Publishers: The Hague, The Netherlands, 1983.
26. White, F.M. *Fluid Mechanics*, 7th ed.; Mc Graw-Hill: New York, NY, USA, 2011.
27. Lauga, E.; Powers, T.R. The hydrodynamics of swimming microorganisms. *Rep. Prog. Phys.* **2009**, *72*, 096601. [[CrossRef](#)]
28. Gray, J. The movement of sea-urchin spermatozoa. *J. Exp. Biol.* **1955**, *32*, 775. [[CrossRef](#)]
29. Rathore, J.S.; Sharma, N.N. Engineering nanorobots: Chronology of modeling flagellar propulsion. *J. Nanotechnol. Eng. Med.* **2010**, *1*. [[CrossRef](#)]
30. Cox, R.G. The motion of long slender bodies in a viscous fluid. Part 1. General theory. *J. Fluid Mech.* **1970**, *44*, 791–810. [[CrossRef](#)]

31. Lighthill, J. Flagellar hydrodynamics. *SIAM Rev.* **1976**, *18*, 161–230. [[CrossRef](#)]
32. Johnson, R.E. Slender body theory for Stokes flow and flagellar hydrodynamics. Ph.D. Thesis, California Institute of Technology, Pasadena, CA, USA, 1977.
33. Johnson, R.E.; Wu, T.Y.T. Hydromechanics of low-Reynolds-number flow. Part 5. Motion of a slender torus. *J. Fluid Mech.* **1979**, *95*, 263–277. [[CrossRef](#)]
34. Johnson, R.E. An improved slender-body theory for Stokes flow. *J. Fluid Mech.* **1980**, *99*, 411–431. [[CrossRef](#)]
35. Chwang, A.T.; Wu, T.Y.T. Hydromechanics of low-Reynolds-number flow. Part 1. Rotation of axisymmetric prolate bodies. *J. Fluid Mech.* **1974**, *63*, 607–622. [[CrossRef](#)]
36. Chwang, A.T.; Wu, T.Y.T. Hydromechanics of low-Reynolds-number flow. Part 2. Singularity method for Stokes flows. *J. Fluid Mech.* **1975**, *67*, 787–815. [[CrossRef](#)]
37. Johnson, R.E.; Brokaw, C.J. Flagellar hydrodynamics. A comparison between resistive-force theory and slender-body theory. *Biophys. J.* **1979**, *25*, 113–127. [[CrossRef](#)]
38. Gray, J.; Hancock, G.J. The propulsion of sea-urchin spermatozoa. *J. Exp. Biol.* **1955**, *32*, 802–814. [[CrossRef](#)]
39. Becker, L.E.; Koehler, S.A.; Stone, H.A. On self-propulsion of micro-machines at low Reynolds number: Purcell’s three-link swimmer. *J. Fluid Mech.* **2003**, *490*, 15–35. [[CrossRef](#)]
40. Collette, Y.; Siarry, P. *Multiobjective Optimization: Principles and Case Studies*, 1st ed.; Decision Engineering; Springer: Berlin/Heidelberg, Germany, 2004.
41. Méndez-Babey, M. Algoritmos Evolutivos y Preferencias del Decisor Aplicados a Problemas de Optimización Multiobjetivo Discretos. Ph.D. Thesis, Departamento de Ingeniería Mecánica, Universidad de Las Palmas de Gran Canaria, Las Palmas de Gran Canaria, Spain, 2008. (In Spanish)